Energy & Environmental Science

A new perspective on the hydraulics of oilfield wastewater disposal: How PTX conditions affect fluid pressure transients that cause earthquakes

Journal:	*Energy & Environmental Science*
Manuscript ID	EE-ART-06-2020-001864
Article Type:	Paper
Date Submitted by the Author:	11-Jun-2020
Complete List of Authors:	Pollyea, Ryan; Virginia Polytechnic Institute and State University, Department of Geosciences Konzen, Graydon; Virginia Polytechnic Institute and State University, Department of Geosciences Chambers, Cameron; Virginia Polytechnic Institute and State University, Department of Geosciences Pritchard, Jordan; Virginia Polytechnic Institute and State University, Department of Geosciences Wu, Hao; Virginia Polytechnic Institute and State University, Department of Geosciences Jayne, Richard; Virginia Polytechnic Institute and State University, Department of Geosciences; Sandia National Laboratories, Applied Systems Analysis and Research Department

Journal Name

ARTICLE TYPE

Cite this: DOI: 00.0000/xxxxxxxxxx

A new perspective on the hydraulics of oilfield wastewater disposal: How PTX conditions affect fluid pressure transients that cause earthquakes†

Ryan M. Pollyea[a,*], Graydon L. Konzen[a], Cameron R. Chambers[a], Jordan A. Pritchard[a], Hao Wu[a], and Richard S. Jayne[a,b]

Received Date
Accepted Date

DOI: 00.0000/xxxxxxxxxx

Pumping oilfield wastewater into deep injection wells causes earthquakes by effective stress change and solid elastic stressing. These processes result from fluid pressure changes in the seismogenic basement, so it is generally accepted that pressure diffusion governs spatiotemporal patterns of induced earthquake sequences. However, new evidence suggests that fluid density contrasts may also drive local-scale (near-well) pressure transients to greater depths than pressure diffusion and over much longer timescales. As a consequence, the pressure, temperature, and composition (PTX) conditions of wastewater and deep crustal (basement) fluids may be fundamental to understanding and managing injection-induced seismicity. This study develops a mechanistic framework that integrates PTX-dependent fluid properties into the generally accepted conceptual model of injection-induced seismicity. Nonisothermal variable-density numerical simulation is combined with ensemble simulation methods to isolate the parametric controls on injection-induced fluid pressure transients. Results show that local-scale, density-driven pressure transients are governed by a combination of fracture permeability and PTX-dependent fluid properties, while long-range pressure diffusion is largely governed by fracture permeability. Considering this new conceptual model in the context geochemical data from oil and gas basins in the United States identifies regions that may be susceptible to persistent density-driven pressure transients.

1 Introduction

There is now scientific consensus that oilfield wastewater disposal in deep injection wells was responsible for the dramatic rise in earthquake frequency across much of the midcontinent United States between 2009 and 2015 (e.g., [1–6]). Induced earthquake sequences are generally explained by effective stress theory because wastewater disposal induces fluid pressure transients that migrate over km scales into seismogenic crust [7]. These fluid pressure transients decrease effective normal stresses acting on faults. For the subset of faults that are optimally oriented to the regional tectonic stress field, earthquakes may occur when effective normal stress falls below the Mohr-Coulomb failure threshold [8].

In addition to effective stress theory, recent research suggests that wastewater injections may also cause elastic stress transfer through solid rock matrix. For example, Goebel *et al.* [7] found that the combined effects of pressure diffusion and solid elastic stressing explain the 40+ km distance separating wastewater disposal wells and the 2016 earthquake sequence in Fairview, Oklahoma. Similarly, Bhattacharya and Viesca [9] show that fluid injections may cause aseismic stress transfer along pressurized faults and over larger lateral distances than is possible by pressure diffusion alone. By separately interrogating the mathematical expressions for pressure diffusion and solid elastic stress transfer, Goebel and Brodsky [10] found that root-time ($\sqrt{t}$) spatial scaling governs induced earthquake sequences that are caused by pressure diffusion (i.e., effective stress change), while earthquakes triggered by solid stress transfer exhibit longer-range spatial scaling in accordance with a power-law ($\sim r^{-1.8}$). This hydromechanical coupling was tested numerically by Zhai *et al.* [11] in a regional-scale wastewater disposal model of Oklahoma, which indicates that pressure diffusion reasonably explains earthquake occurrence from 2008 to 2017, while solid elastic stressing increases the seismic hazard by a factor of 2 to 6 times.

Although solid elastic stress transfer is one mechanistic process that explains long-range earthquake triggering, Peterie *et al.* [12] reported observations of increasing fluid pressure within deep observation wells located >90 km from high-rate injection wells

[a] *Department of Geosciences, Virginia Polytechnic Institute & State University, Blacksburg, Virgina, USA.*
[b] Present address: *Applied Systems Analysis and Research Department, Sandia National Laboratory, Albquerque, New Mexico, USA.*
† Electronic Supplementary Information (ESI) available: Text S1, Figure S1-S2. See DOI: XX.XXXX/XXXXXXXX.
∗ Corresponding author: Tel: +1 540 231 7929; E-mail: rpollyea@vt.edu

at the Oklahoma-Kansas border. Moreover, these observations occurred contemporaneously with earthquake occurrence [12]. To explain this phenomenon, Pollyea [13] used numerical simulation to show that the hydrogeologic principle of superposition is the mechanistic process that explains how pressure fronts from multiple wells interact and merge to locally increase the hydraulic gradient, thus driving long-range pressure transients. Together, these studies show that fluid pressure fronts from clusters of high-rate wastewater disposal wells can travel much greater distances than previously considered possible.

There is now substantial evidence that the combination of effective stress change and solid elastic stressing explain the relationship between wastewater disposal operations and induced earthquake sequences. From a conceptual perspective, wastewater injection induces a pressure diffusion front that (i) decreases effective stress within its spatial footprint and (ii) transfers elastic stress through the solid rock matrix at longer spatial scales [7]. This means that fluid pressure transients are the first-order process governing induced earthquakes because effective stress change and solid elastic stressing are both dependent on loading conditions imposed by wastewater injection. However, despite the theoretical evidence to support these processes, pore pressure in the seismogenic basement is rarely measured directly. As a result, groundwater models are commonly implemented to show that pressure diffusion fronts tend to match earthquake occurrence in both space and time (e.g., [5,7,11,14]).

As groundwater models continue to demonstrate the relationship between wastewater disposal and earthquakes, there is increasing interest in how these models represent the seismogenic basement ($\geq$ 3 km). At these depths, PTX (pressure, temperature, composition) conditions vary substantially; however, numerous modeling studies assume isothermal geologic conditions, which implicitly assumes that pressure diffusion is the only mechanistic process that causes effective stress change [5,7,11,14–22]. This assumption was recently challenged by Pollyea *et al.* [23], who found that wastewater composition on the Anadarko Shelf in northern Oklahoma and southern Kansas comprises much higher total dissolved solids (TDS) concentration ($\sim$175,000 - 235,000 ppm) than fluids in the seismogenic basement ($\sim$107,000 ppm). As a result, high-TDS wastewater sinks, displaces lower TDS basement fluids, and increases fluid pressure (and decreases effective stress) due to the density differential between wastewater and basement fluids [23]. These density-driven pressure transients are independent of wellhead pressure, which explains why mean annual earthquake depth continues increasing in northern Oklahoma despite substantial injection rate reductions [23]. Moreover, density-driven pressure transients may continue sinking and pressurizing basement rocks for years after injection operations cease, which is likely to prolong earthquake hazard. As a consequence, PTX conditions of both wastewater and basement fluids may play a fundamental role in earthquake occurrence during periods of injection volume reductions when wastewater is characterized by $\gtrsim$200,000 ppm TDS concentration, e.g., in Oklahoma from 2016 to present.

The generally accepted conceptual model for injection-induced seismicity is that pressure diffusion decreases effective stress within its spatial footprint, while also driving solid elastic stressing ahead of the pressure front. However, this conceptual model is incomplete because there is now compelling evidence that high-TDS wastewater disposal causes density-driven pressure transients that decrease effective stress within the seismogenic basement. Moreover, recent studies that independently interrogate diffusion-controlled [13] and density-driven pressure transients [23] show that each mechanistic process operates on different spatial and temporal scales. Specifically, pressure fronts caused by diffusion occur rapidly and extend to long radial distances from injection wells [12], but collapse soon after injection operations cease [13]. In contrast, density-driven pressure transients occur in localized regions below injection wells and continue increasing fluid pressure over much longer time scales than pressure diffusion [23]. The study presented here combines these processes into a unified mechanistic framework for understanding the hydraulics of oilfield wastewater disposal. In doing so, ensemble simulation methods are employed by deconstructing hydraulic diffusivity into its parametric form in order to isolate the hydraulic, thermal, and geologic controls on both diffusion-controlled (long-range) and density-driven (local-scale) pressure transients. Results from this study add an important new perspective on the hydraulic processes governing injection-induced pressure transients, and thus injection-induced seismicity.

2 Methods

Injection-induced pressure transients are known to propagate over km-scales through the seismogenic crust [5,7]. At these scales, there is substantial uncertainty in both geologic and fluid properties, which vary as temperature and pressure increase with depth [24,25]. This uncertainty is compounded because there is now evidence that wastewater fluid composition plays an important role in the process of density-driven pressure transients. Moreover, operational procedures may also introduce uncertainty because because oilfield wastewater is likely to cool during production, separation, and transport, which alters its temperature-dependent fluid properties (i.e., density and viscosity) prior to reinjection. Despite these many sources of uncertainty, there has not yet been a systematic analysis of the relationship between the geologic properties and PTX-dependent fluid properties that govern injection-induced fluid pressure transients. To bridge this knowledge gap and isolate the hydraulic, thermal, geochemical and geologic controls on injection-induced pressure transients, this study combines non-isothermal, variable density groundwater modeling with ensemble simulation analytics to model and interrogate 120 uniquely parameterized oilfield wastewater models of the same injection scenario.

Model Scenario. The model scenario represents a typical high-rate (2,080 m^3 day^{-1}, 13,000 bbl day^{-1}) injection well operating on the Anadarko Shelf in northern Oklahoma, USA. In this region, oilfield brine produced from the Mississippi Lime formation is characterized by mean TDS concentration of $\sim$207,000 ppm [26]. The injection well is completed within the upper half of the Arbuckle formation, which is a regionally confined reservoir that occurs between $\sim$1,900 and 2,300 m depth and is jux-

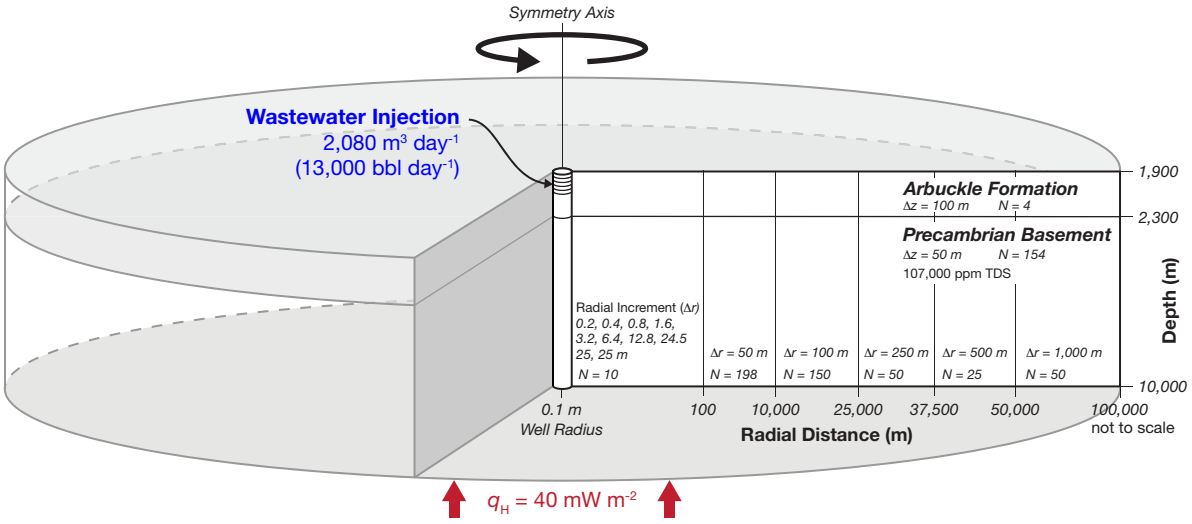

Fig. 1 Schematic illustration of the model scenario utilized for this study. The domain is a 3-D radially-symmetric volume with vertical grid discretization (Δz) of 100 m in the Arbuckle formation and 50 m in the Precambrian basement. Radial discretization (Δr) increases systematically from the central injection well, where wastewater is injected in the upper 200 m of the Arbuckle formation. Lateral boundaries are Dirichlet conditions. Upper and lower boundaries are adiabatic to fluid, except for the lower basal boundary which imposes a 40 mW m^{-2} heat flux (q_H).

taposed with the underlying crystalline basement[27]. Each model domain is a 3-D cylindrical volume with axial symmetry, which reduces the dimensionality to 2-D (Fig. 1). The model domain is discretized in the radial direction with systematically increasing grid cell dimension up to the maximum radial extent of 100 km, which approximates a semi-infinite far-field dimension. Vertical grid discretization in the Arbuckle formation comprises 100 m increments, while the underlying basement is discretized in 50 m increments to a maximum depth of 10 km. Initial geologic conditions represent gravity and thermal equilibrium for: (i) basement fluid composition of 107,000 ppm TDS[26], (ii) a fixed upper boundary of 18 MPa fluid pressure and 45°C, and (iii) the 40 mW m^{-2} regional geothermal heat flux for northern Oklahoma[28]. These conditions were calculated with the TOUGH3 numerical simulation code[29], and result in a geothermal gradient of ~18°C km^{-1} and fluid pressure gradient of ~10 MPa km^{-1} (Fig. 2A). The corresponding density gradient decreases non-linearly through the basement with a range of ~1,070 to ~995 kg m^{-3} (Fig. 2B).

Hydraulic Properties. Over the last decade, hydraulic diffusivity is perhaps the most commonly implemented reservoir parameter for describing the hydraulic characteristics of the seismogenic basement (e.g.,[5,11,22]). In saturated isotropic porous geologic media, hydraulic diffusivity (D_H, m^2 s^{-1}) is defined as the ratio of hydraulic conductivity (K, m s^{-1}) to specific storage (S_s, m^{-1}),

$$D_H = \frac{K}{S_s}, \tag{1}$$

and scales the temporal pressure diffusion characteristics of porous geologic media. For underground fluid injections, the magnitude and extent of fluid pressure propagation are modulated by the rate at which pre-existing fluids are displaced, so reservoirs characterized by larger diffusivity can readily accept fluid injections without substantial fluid pressure build-up.

Hydraulic diffusivity is a highly intuitive conceptual descriptor of geologic fluid systems that is readily implemented in the groundwater flow equation, but it also simplifies important information about material properties that govern geologic fluid systems. Specifically, the hydraulic conductivity (K in Eq. 1) of saturated porous media can be described as,

$$K = \frac{k\rho_f g}{\mu}, \tag{2}$$

where, k is intrinsic permeability (m^2), ρ_f is fluid density (kg m^{-3}), g is acceleration due to gravity (m s^{-2}), and μ is dynamic viscosity (kg m s^{-1})[30]. From Equation 2, it is clear that hydraulic conductivity varies with fluid density and viscosity, which are both dependent on PTX conditions. The specific storage coefficient (S_s in Eq. 1) for saturated porous media is defined as,

$$S_s = \rho_f g(\beta_r + \phi\beta_f) \tag{3}$$

where, β_r and β_f are rock and fluid compressibility (Pa^{-1} or m s^2 kg^{-1}), respectively, and ϕ is porosity (-)[30]. As a result, specific storage also varies with PTX conditions owing to its dependence on fluid density and fluid compressibility. However, this density dependence drops out of hydraulic diffusivity when Equations 2 and 3 are substituted into Equation 1,

$$D_H = \frac{k}{\mu(\beta_r + \phi\beta_f)}. \tag{4}$$

By assuming that the product $\phi\beta_f$ is very small in comparison to β_r, then Equation 4 reduces to

$$D_H \approx \frac{k}{\mu\beta_r}, \tag{5}$$

which means that hydraulic diffusivity is a function of both geology (k and β_r) and fluids (μ). This relationship shows that hydraulic diffusivity is inversely proportional to fluid viscosity,

which varies four-fold over the 8 km depth interval considered in this study (Fig. 2B). Moreover, it is generally accepted that permeability tends to decay with depth, and several studies convincingly argue that bulk permeability of the seismogenic crust ranges between 10^{-14} and 10^{-17} m^2 [24,31,32]. Because hydraulic diffusivity depends on both fluid viscosity and permeability, it follows that hydraulic diffusivity varies with depth due to the natural geothermal gradient and the depth-dependence of permeability. Moreover, wastewater that is injected with different composition and temperature than host rock fluids may cause hydraulic diffusivity to change dynamically as wastewater infiltrates the basement.

For this study, the wastewater disposal scenario is repeated for 120 individual models, each comprising unique combinations of basement fracture permeability, basement fracture compressibility, wastewater temperature, and wastewater TDS concentration. This 4-D parameter space is implemented by initially discretizing the basement subdomain as a dual continua with 98 vol.% rock matrix and 2 vol.% fracture. Basement rock matrix is specified with uniform permeability (k_m) of 1×10^{-20} m^2, while basement fracture permeability (k_f) decays with depth (z) according to the Manning and Ingebritsen [24] power law model: $k_f(z) = k_0(z/z_0)^{-3.2}$. To implement this permeability model for the ensemble simulation, z_0 is specified as depth of the Arbuckle-basement contact (2,300 m), and four different k_0 scenarios are considered (Fig. 3A). The volume-weighted effective (bulk) permeability for these scenarios ranges from 1×10^{-14} to 2×10^{-18} m^2, which is congruent with both field measurements and theoretical constraints for crustal-scale effective permeability [24,31,32]. The ensemble parameter space also comprises six compressibility (β_r) values for the basement fracture continuum that range from 1×10^{-9} to 5×10^{-12} Pa^{-1}, which represents compliant to effectively incompressible fractures.

To account for thermal and compositional variability of oilfield brine, this study also isolates for wastewater temperature and wastewater TDS concentration. In northern Oklahoma, oilfield brine is characterized by ~207,000 ppm TDS [23]; however, injection temperature is *a priori* unknown. To bound this uncertainty, the simulation ensemble developed here considers three scenarios for the injection temperature of wastewater: 10, 25 and 40°C. These scenarios are based on fluid composition of 207,000 ppm TDS. The upper end of this range (40°C) reflects brine temperature corresponding to $\gtrsim 1.5$ depth, i.e., deep brine that is reinjected soon after production. The lower end of this range corresponds with the average low temperature in Oklahoma and reflects oilfield brine that cools substantially during above ground transport and storage. In order to identify the relationship between wastewater TDS concentration and the occurrence of density-driven pressure transients, two additional wastewater composition scenarios are tested: 107,000 ppm and 157,000 ppm TDS, each of which is modeled at 25°C. These scenarios provide a lower bound for wastewater composition that is identical to basement composition (107,000 ppm TDS), as well as a middle scenario that reflects variability in oilfield brine composition [26].

In the context of hydraulic diffusivity, this 4-D parameter space spans a wide range of plausible permeability and compressibility values, while bounding compositional and thermal variability of oilfield wastewater. The complete parameter space is shown graphically in Figures 3B and 3C, along with corresponding hydraulic diffusivity values (Eq. 5) for each wastewater temperature (Fig. 3B) and composition (Fig. 3C) scenario at pressure conditions representative of the Arbuckle-basement interface. To illustrate the thermal effects on hydraulic diffusivity through the basement thickness, Figure 3A also presents a comparison between fracture permeability and fracture hydraulic diffusivity for each permeability scenario.

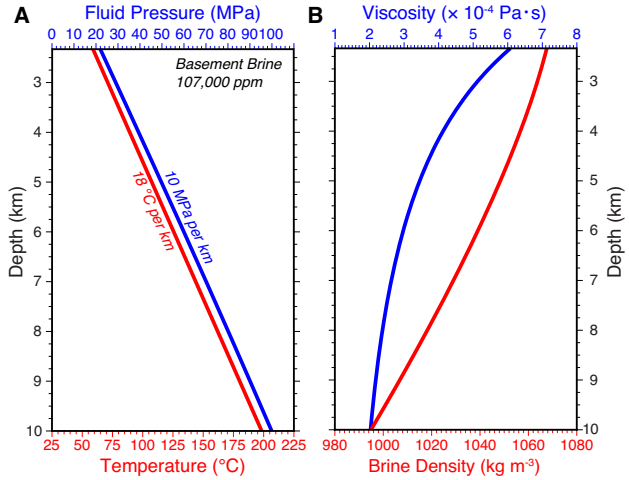

Fig. 2 Initial basement conditions for the wastewater disposal scenario implemented in this study. Fluid pressure (blue) and temperature (red) gradients are shown in A for 107,000 ppm TDS with density (red) and viscosity (blue) gradients are shown in panel B.

Boundary Conditions and Simulation. Individual wastewater disposal simulations (N = 120) were completed for each parameter combination shown in Figures 3B and 3C. For these simulations, the upper boundary is adiabatic because the Arbuckle formation is known to be regionally confined by overlying Ordovician to Devonian shale formations [27]. The radial boundary corresponding to 100 km from the central injection well is specified as Dirichlet to maintain the hydraulic and thermal gradients in the far field. The basal boundary imposes the 40 mW m^{-2} geothermal heat flux for northern Oklahoma [28]. For each simulation, wastewater is injected for ten years at a rate of 2,080 m^3 day^{-1} (13,000 bbl day^{-1}). This injection rate corresponds with a typical high-rate injection well on the Anadarko Shelf of northern Oklahoma and southern Kansas [6]. Following the ten-year injection period, the model continues for another 40 years to evaluate fluid pressure recovery. The code selection for this study is TOUGH3 [29] compiled with the equation of state module for non-isothermal mixtures of pure water and brine . This formulation assumes that brine TDS are NaCl, and we implement the TOUGH3 option for fluid mixing by molecular diffusion. A summary of the governing equations and numerical solution scheme are presented as Electronic Supplementary Materials†. Table 1 presents the static parameters utilized for this study.

Response Surface Analysis. The complete simulation ensemble comprises 120 wastewater disposal models with unique

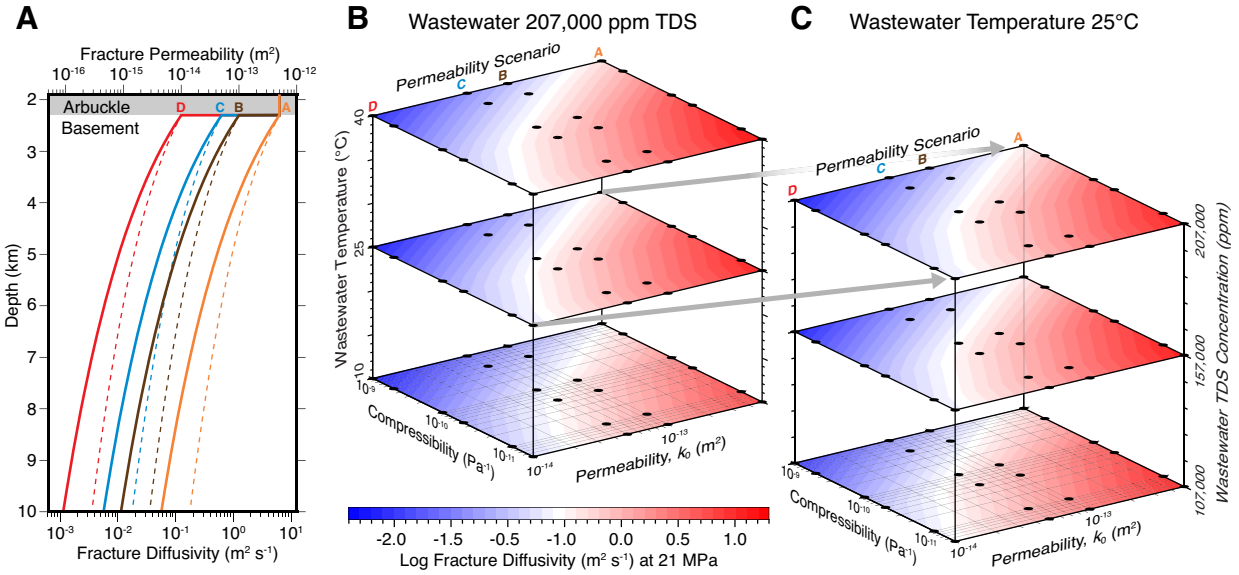

Fig. 3 Permeability scenarios and parameter space tested for this ensemble simulation study. Panel A shows basement fracture permeability scenarios (solid lines, labeled A - D) that are based on the depth-decaying permeability model by Manning and Ingebritsen [24]. Dashed lines are fracture diffusivity corresponding to each permeability scenario for 107,000 ppm TDS basement brine, basement compressibility of 1×10^{-10} Pa^{-1}, and initial conditions in Figure 2A. The complete parameter space is presented in panels B and C, where black circles denote unique combinations of basement fracture permeability, basement compressibility, and either wastewater temperature (Panel B) or wastewater TDS concentration (Panel C). Note that all parameter combinations shown in B are for wastewater comprising 207,000 ppm TDS and all parameter combinations shown in C are for wastewater temperature of 25°C, thus middle slice in B is the same as top slice in C (as denoted by gray arrows). Color palette in B and C reflects hydraulic diffusivity (Eq. 5) for each parameter combination at fluid pressure corresponding to the Arbuckle-basement contact (21 MPa).

combinations of wastewater temperature, wastewater composition, depth-decaying basement permeability, and basement compressibility (Fig. 3B,C). Because visualizing 4-D data is cognitively challenging, simulation results are analyzed using three-dimensional response surface methods [33]. This approach contours a specific model feature (e.g., maximum distance to 10 kPa pressure front) across two-dimensional parameter maps and then stacks three 2-D maps on vertical axis. For this study, all response surface plots are organized as shown in Figures 3B and 3C, where permeability and compressibility are the horizontal axes and either wastewater temperature or composition is the vertical axis. Response surface maps of selected model features are contoured for each wastewater scenario using all combinations of fracture compressibility (β_r) and permeability scenario, the latter of which is identified on Figures 4-9 by fracture permeability at the Arbuckle-basement interface (k_0).

3 Results

Long-range, diffusion-controlled pressure transients. It is well known that individual high-rate wastewater injection wells can drive fluid pressure transients to radial distances exceeding 10-15 km (e.g., [34,35]). To isolate the parametric controls on this phenomenon, Figures 4A and 5A present response surface analyses for the maximum radial distance between the injection well and the 10 kPa pressure front after 10 years of wastewater injection. The 10 kPa pressure front is chosen for this analysis because it is generally considered the minimum stress-change to reactivate critically-stressed faults [36]. Across the complete simulation ensemble, the 10 kPa pressure front ranges from 6 to 29 km lateral distance from the injection well after 10 years of injection. Response surface analyses reveal the intuitive finding that the maximum lateral extent of the 10 kPa pressure front increases systematically with decreasing fracture permeability; however, this analysis also finds that long-range pressure transients (i) are insensitive to wastewater temperature (Fig. 4A), (ii) increase modestly with decreasing wastewater TDS concentration (Fig. 5A), and (iii) are slightly inhibited when the fracture network is compliant ($\beta_r \sim 10^{-9}$) and fracture permeability is low ($k_0 \sim 10^{-14}$ m^2). This is shown in Figures 4A and 5A as gradients that are strongly oriented in the direction of decreasing fracture permeability with minor variations along the compressibility and wastewater temperature or composition axes. From a qualitative perspective, this result reflects the well-known phenomenon that fractured crystalline rocks are highly effective for transmitting fluids, but generally maintain little excess storage capacity.

Although this previous result is somewhat intuitive, individual results for simulations bounding the parameter space show that the shape of the 10 kPa pressure front is strongly dependent on the basement permeability structure (Figs. 4B-G & 5B-G). Specifically, long-range fluid pressure transients for the low permeability scenarios ($k_0 = 1 \times 10^{-14}$ m^2) reach their maximum lateral extent at shallow depths (2 – 4 km in this model) because the depth-decaying permeability structure impedes lateral pressure propagation at greater depth (Figs. 4D,E & 5D,E). In contrast, the 10 kPa pressure fronts for the intermediate permeability scenarios ($k_0 = 1 \times 10^{-13}$ m^2 and $k_0 = 5 \times 10^{-14}$ m^2) propagate uniformly throughout the basement thickness (Fig. 4C,F & 5C,F), while the 10 kPa pressure fronts for the high-permeability sce-

Table 1 Static model parameters

	k-matrix m^2	k-fracture m^2	ϕ –	ρ_f kg m^{-3}	β_r Pa^{-1}	k_T W m^{-1} °C^{-1}	c_p J kg^{-1} °C^{-1}	D m^2 s^{-1}
Arbuckle	5×10^{-13}	–	0.1	2,500	1.7×10^{-10}	2.2	1,000	–
Basement	1×10^{-20}	Fig 3A	0.1^c,0.02^d	2,080	Fig 3B	2.2	1,000	–
Brine	–	–	–	variable	–	–	–	1.1×10^{-9}

k_T-thermal conductivity. c_p-specific heat. D-diffusion coefficient. c-fracture porosity. d-matrix porosity.

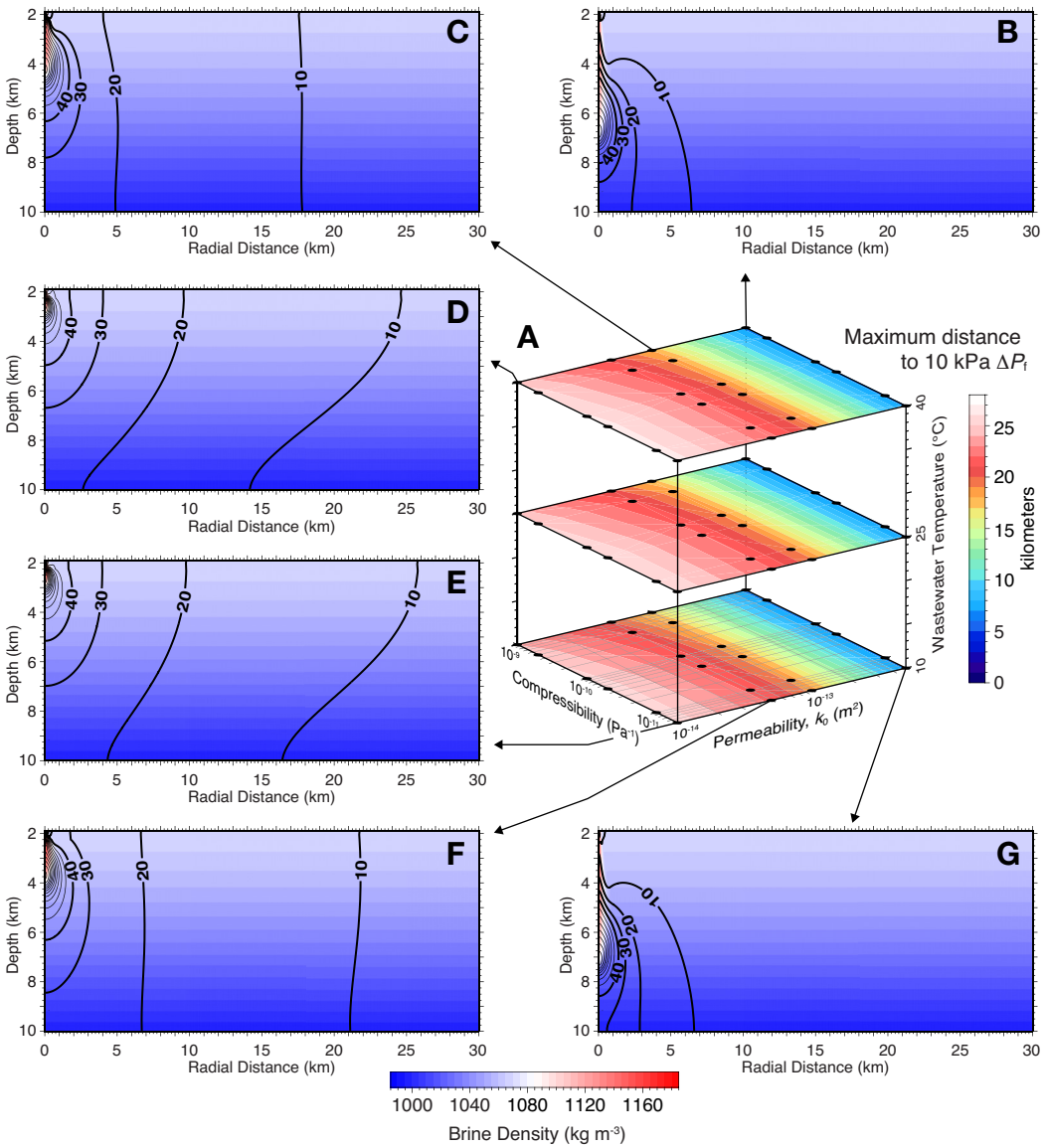

Fig. 4 Response surface analysis (A) for the maximum radial distance (km) from the injection well to the 10 kPa pressure front after 10 years of injection for wastewater comprising 207,000 ppm TDS brine at 10, 25, and 40°C. Panels B - G illustrate individual simulation results for models that bound the parameter space; black contour lines denote fluid pressure change (ΔP_f) in kPa and background shading is brine density. Contour lines greater than 40 kPa are presented with lighter stroke to facilitate visualization. Note that 10 kPa pressure front migrates substantially longer radial distances than the wastewater plume. Detailed sections for each wastewater plume in B - G are shown in Figure 6.

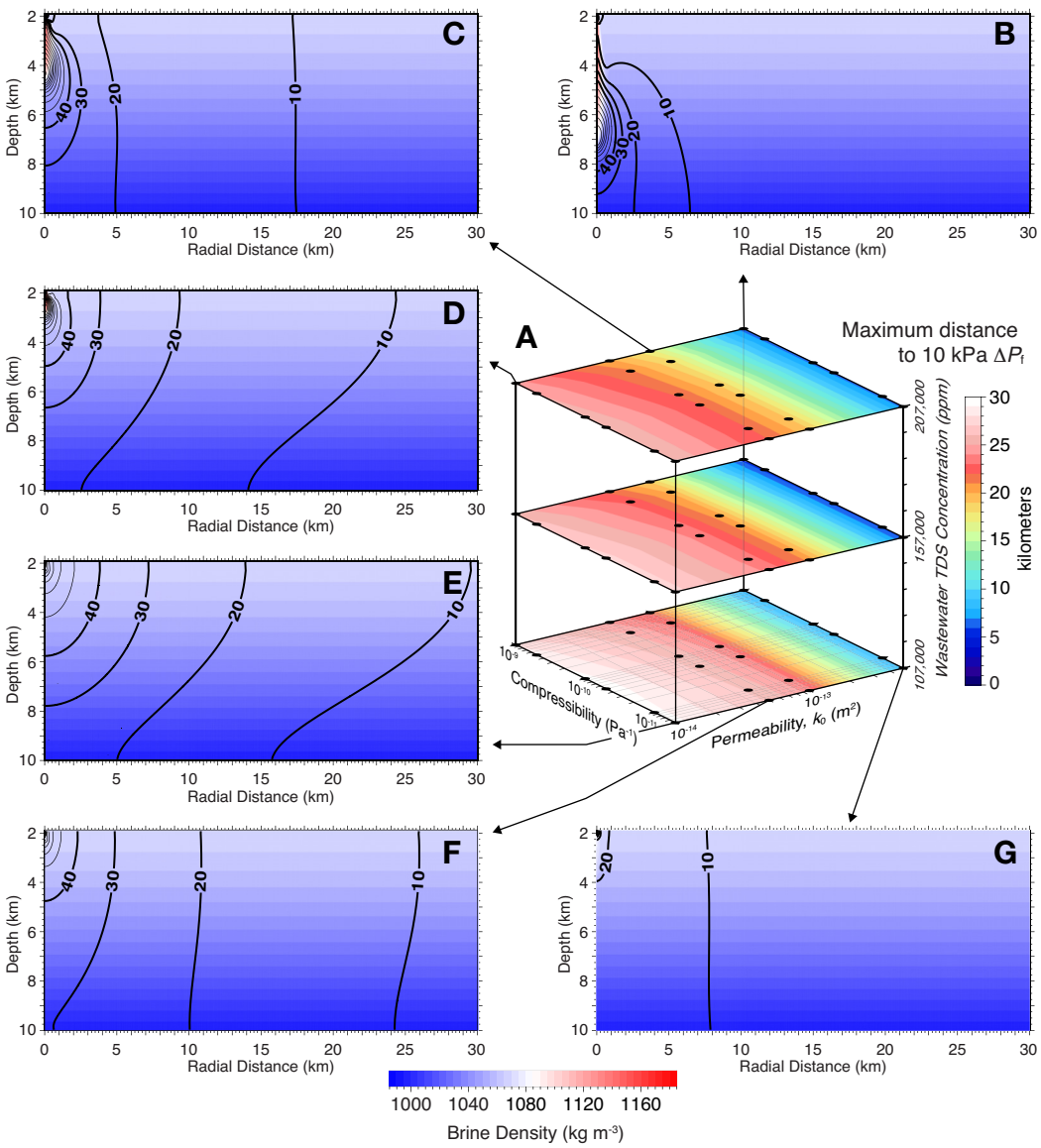

Fig. 5 Response surface analysis (A) for the maximum radial distance (km) from the injection well to the 10 kPa pressure front after 10 years of injection for wastewater at 25°C and brine composition of 107,000, 157,000 and 207,000 ppm TDS. Panels B – G illustrate individual simulation results for models that bound the parameter space; black contour lines denote fluid pressure change (ΔP_f) in kPa and background shading is brine density. Contour lines greater than 40 kPa are presented with lighter stroke to facilitate visualization.

narios ($k_0 = 5 \times 10^{-13}$ m^2) reach their maximum lateral extent at much greater depths (Fig. 4B,G & 5B); however, this latter trend does not occur for the high permeability model with 107,000 ppm TDS wastewater (Fig. 5G).

The tendency for the high permeability scenarios to cause lateral pressure migration at greater depths results from the relationship between fracture permeability and high-TDS wastewater. At 25°C and 21 MPa fluid pressure, wastewater comprising 207,000 ppm TDS has a fluid density of ~ 1157 kg m^{-3}, while the corresponding density for 107,000 ppm TDS basement fluid is ~ 1081 kg m^{-3} [25]. This fluid density contrast allows the wastewater to sink rapidly through high permeability fractures and displace basement fluids, which increases fluid pressure below the injection well and drives a short-range pressure diffusion front laterally. As high-density wastewater sinks deeper into the basement, formation fluids are drawn in from above which results in a zone of underpressure near the injection well. In Oklahoma, this process may explain the phenomenon in which high-rate wastewater injection wells operate in close proximity without pumping (i.e., gravity-fed injections) [14]. However, density-driven fluid flow is inhibited when wastewater and basement fluids comprise the same TDS concentration. This explains why the 10 kPa pressure front advances uniformly through the basement for the high permeability model with 107,000 ppm TDS wastewater (Fig. 5G).

Local-scale, density-driven pressure transients. The relationship between fluid composition and earthquake occurrence was first identified by Pollyea *et al.* [23], which used numerical simulation to show that density-driven pressure transients sink at the same rate as mean annual earthquake depths increase within several Oklahoma counties. The study also found that the relative proportion of high-magnitude earthquakes increases at 8+ km depth. While the earthquake rate at 8+ km depth is small in comparison to more shallow depths, density-driven pressure transients may persist in the seismogenic zone over much longer time scales than pressure fronts governed by pressure diffusion alone. As a result, density-driven pressure transients may prolong earthquake hazard in regions where wastewater is characterized by substantially higher TDS concentration than fluids in the seismogenic basement.

To explore parametric controls on density-driven pressure transients, Figures 6A and 7A present response surface analyses for the maximum depth of 40 kPa pressure change after 10 years of injection at 2,080 m^3 day^{-1} (13,000 bbl day^{-1}). The 40 kPa pressure front is considered for this analysis because its depth is strongly influenced by sinking, high-density wastewater during the 10-year injection period (Fig. 6C-G, 7B-D). As with lateral long-range (diffusion-controlled) pressure transients, this analysis reveals that basement permeability structure is the first-order control on the depth to which density-driven pressure transients may sink. For wastewater composition of 207,000 ppm TDS, the 40 kPa pressure front reaches ~5 km, ~6 km, and ~7 km depth after 10 years for the low, intermediate, and high permeability scenarios, respectively (Fig. 6B-G). These results show that density-driven pressure transients also emerge when wastewater comprises 157,000 ppm TDS (Fig. 7B-D); however, the depth to the 40 kPa pressure front is ~1 - 1.5 km less than the corresponding high-TDS injection scenarios. Because the 40 kPa pressure front is driven largely by sinking, high-TDS wastewater, the density differential between wastewater and basement fluids is a fundamental control on density-driven pressure transients. For the high-TDS wastewater scenarios (207,000 ppm), the density differential between 25°C wastewater and basement fluids is ~76 kg m^{-3} at the Arbuckle-basement interface, but this difference reduces to ~ 37 kg m^{-3} for wastewater comprising 157,000 ppm TDS. This result implies that even modest density differences may cause density-driven pressure transients to develop locally below injection wells when permeability is high enough to permit density-driven fluid flow into the basement. In contrast, the simulation ensemble also reveals that density-driven pressure transients do not occur when (i) permeability is insufficient ($\lesssim 10^{-14}$ m^2) to allow density-driven fluid flow into the basement (Fig. 6B,E & 7B,E) and (ii) the density contrast between wastewater and basement fluids is insufficient to cause density-driven fluid flow (Fig. 7E-G). As a consequence, fluid pressure transients are driven primarily by pressure diffusion when basement fracture permeability is low (e.g., $\lesssim 5 \times 10^{-14}$ m^2) and/or wastewater and basement fluids comprise similar fluid density.

Closer inspection of Figure 6B-G reveals that wastewater injection temperature imposes a second-order control on the depth and magnitude of density-driven pressure transients because the 40 kPa pressure front becomes systematically deeper as wastewater injection temperature decreases (Fig. 6A). This phenomenon occurs because the wastewater density is ~1148 kg m^{-3} at 40°C and 21 MPa, but increases to ~1164 kg m^{-3} at 10°C and 21 MPa. The additional load imposed by lower temperature wastewater increases the fluid potential causing the wastewater plume to sink deeper into the seismogenic zone. These thermal effects further reinforce the development of density-driven pressure transients because fluid density in the basement decreases with depth due to the geothermal gradient (Fig. 2B). As a result, the fluid density contrast is maintained as wastewater sinks deeper into the seismogenic basement. To illustrate this phenomenon, individual simulation results for high permeability scenarios with 207,000 ppm TDS wastewater show that the maximum fluid pressure change (ΔP_f) is 110 kPa between 6.75 and 7.25 km depth for wastewater injection temperature of 10°C (Fig. 6G); whereas, the maximum ΔP_f is 100 kPa between 6.5 and 7 km depth when wastewater is 40°C (Fig. 6D). This general pattern is also apparent for the corresponding intermediate permeability scenarios, but low permeability scenarios prevent density-driven pressure transients from entering the basement within the first 10 years of injection (Fig. 6B,E).

In aggregate, this study finds that density-driven pressure transients may cause effective stress change in the seismogenic basement when (i) basement fracture permeability exceeds $\sim 5 \times 10^{-14}$ m^2 at the basement contact and (ii) the fluid density contrast between wastewater and basement fluids exceeds ~37 kg m^{-3}. Results for the high- and intermediate-permeability scenarios tested here can be further generalized as (i) basement fracture permeability and fluid density contrast are first-order controls on the depth interval and magnitude density-driven pressure

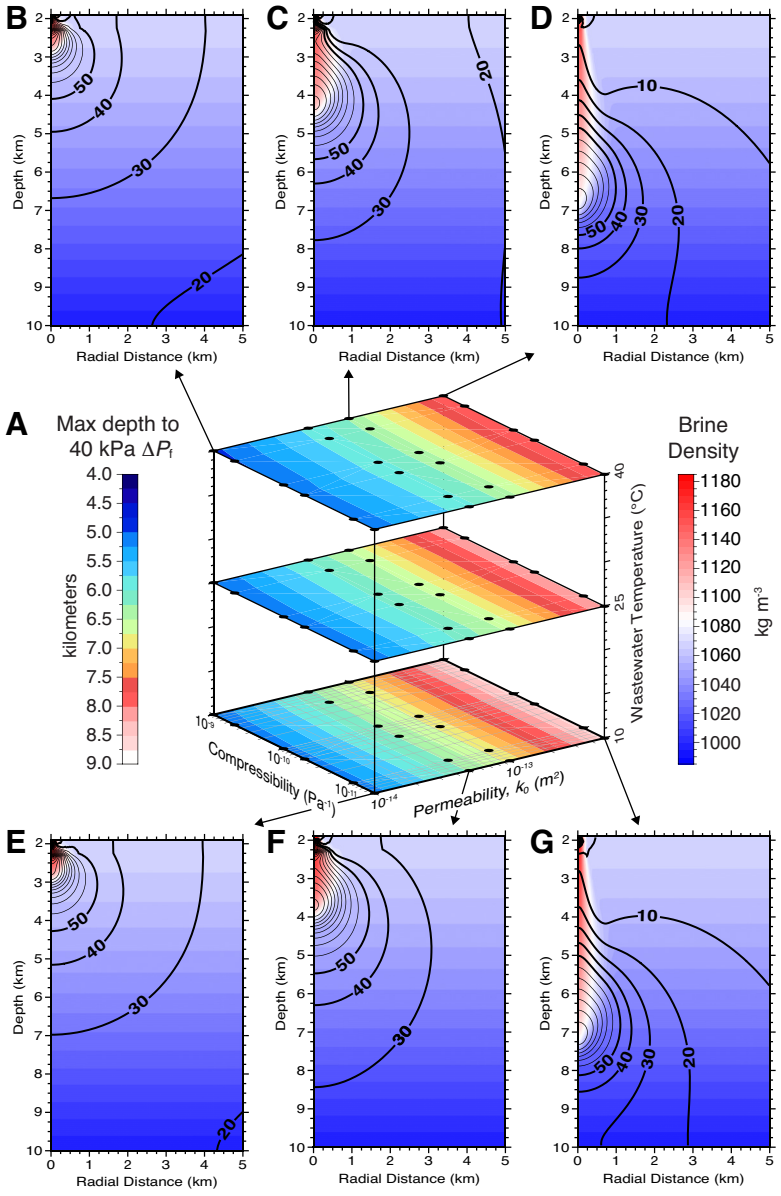

Fig. 6 Response surface analysis (A) for the maximum depth (km) of the 40 kPa pressure front after 10 years of injection with wastewater comprising 207,000 ppm TDS brine at 10, 25, and 40°C. Panels B – G illustrate individual simulation results for models that bound the parameter space; black contour lines denote fluid pressure change (ΔP_f) in kPa and background shading is brine density. Contour lines greater than 50 kPa are presented with lighter stroke to facilitate visualization.

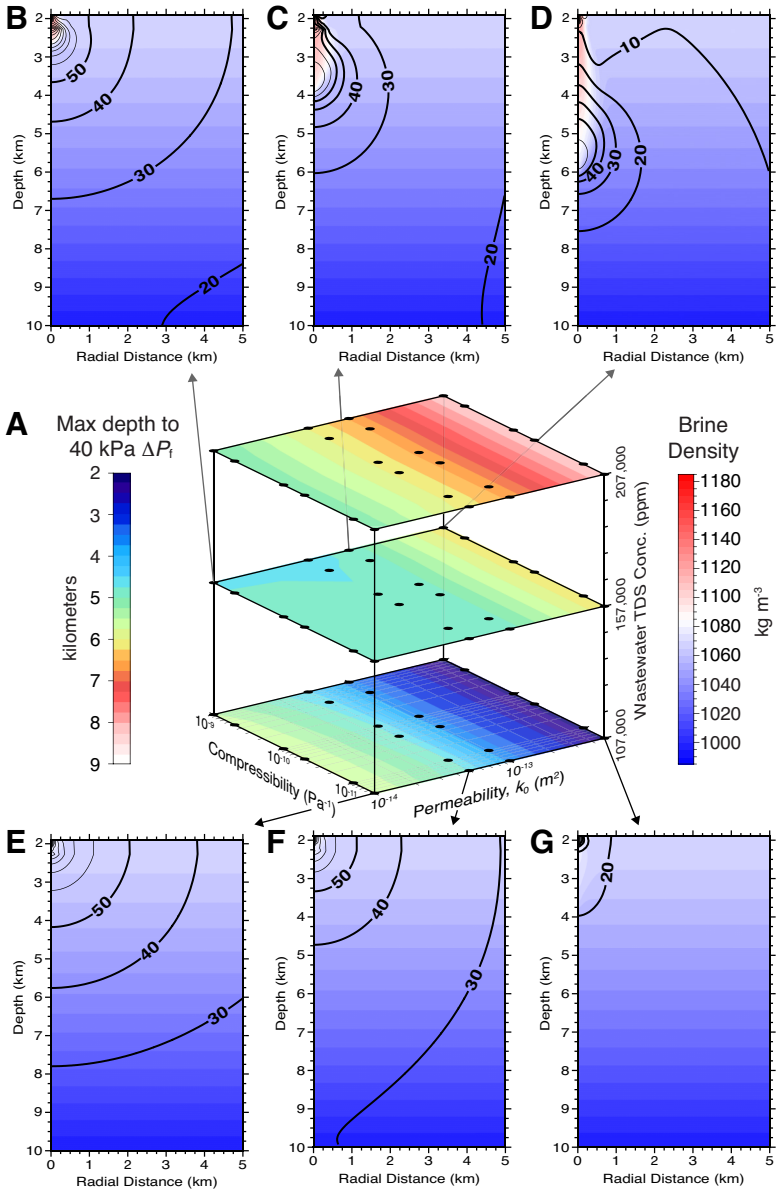

Fig. 7 Response surface analysis (A) for the maximum depth (km) of the 40 kPa pressure front after 10 years of injection for wastewater at 25°C and brine composition of 107,000, 157,000 and 207,000 ppm TDS. Panels B – G illustrate individual simulation results for models that bound the parameter space; black contour lines denote fluid pressure change (ΔP_f) in kPa and background shading is brine density. Contour lines greater than 50 kPa are presented with lighter stroke to facilitate visualization.

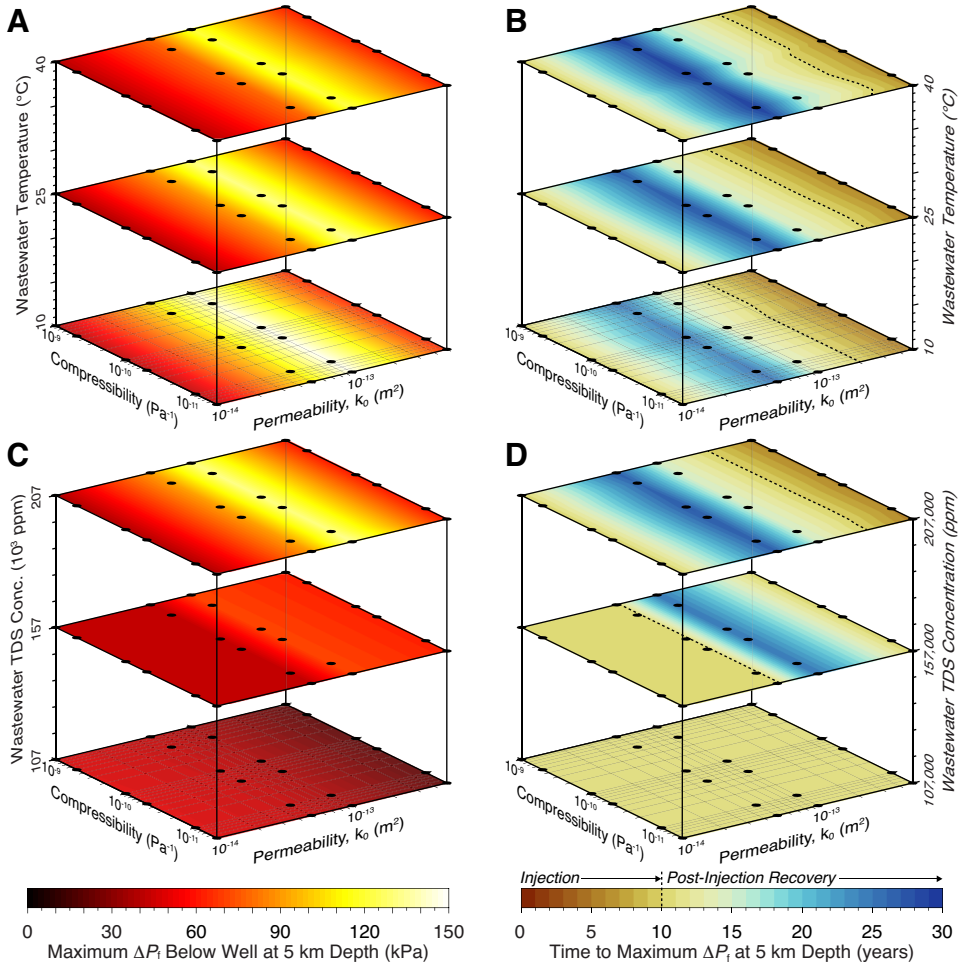

Fig. 8 Magnitude and timing of maximum fluid pressure change (ΔP_f) below the injection well at 5 km depth. (A) Maximum ΔP_f for wastewater comprising 207,000 ppm TDS at 10, 25, and 40°C with (B) corresponding time to reach max ΔP_f. (C) Maximum ΔP_f for wastewater at 25°C and 107,000, 157,000 and 207,000 ppm TDS with (D) corresponding time to reach max ΔP_f. For B and D, dashed black lines denote 10 years, which is the duration of simulated wastewater injection. For wastewater comprising 207,000 ppm TDS (A,B), maximum ΔP_f occurs (i) during the injection period when $k_0 \gtrsim 2 \times 10^{-13}$ m^2; (ii) after the injection period when $2 \times 10^{-13} \lesssim k_0 < 1 \times 10^{-14}$ m^2; and (iii) at the same time as injections cease when $k_0 \leq 1 \times 10^{-14}$ m^2. For wastewater comprising 107,000 and 157,000 ppm TDS at 25°C (C,D), maximum ΔP_f occurs when injections cease for all permeability scenarios except $k_0 = 1 \times 10^{-14}$ m^2 at 157,000 ppm TDS.

transients, (ii) wastewater injection temperature imposes second-order effects with cooler (higher density) wastewater driving pressure transients deeper and to higher magnitude, and (iii) density-driven pressure transients are insensitive to basement compressibility.

Post-injection pressure recovery. The rate of injection-induced earthquakes in Oklahoma has fallen each year since 2015[6]; however, wastewater disposal operations have been widespread throughout the region since 2009[3,6]. Because oilfield brine in northern and eastern Oklahoma is characterized by TDS concentration between 175,000 and 235,000 ppm[26], the persistence of density-driven pressure transients may delay the time scale over which seismicity reaches background levels[23]. To understand the temporal dimension of density-driven pressure transients, Figure 8 presents response surface analyses for maximum ΔP_f recorded directly below the injection well at 5 km depth, along with corresponding response patterns for the time at which maximum ΔP_f occurs. At 5 km depth, maximum ΔP_f ranges from 20 to 150 kPa (Fig. 8A,C); however, the response patterns reveal a number of counterintuitive findings. For example, the maximum ΔP_f at 5 km depth occurs for model scenarios in which wastewater composition is 207,000 ppm TDS, injection temperature is 10°C and k_0 is 1×10^{-13} m^2. This result is congruent with high TDS and low temperature (thus higher density) wastewater locally increasing pressure magnitude below injection wells, but it is not readily apparent why maximum ΔP_f at 5 km depth occurs at one of the intermediate permeability scenarios.

The phenomenon in which ΔP_f at 5 km depth is greatest for intermediate permeability scenarios can be explained by decoupling the two different pressure propagation mechanisms operating within the wastewater disposal system: (i) wellhead pressure diffusion and (ii) advective transport of high-density brine. To do so, time-series ΔP_f data were recorded below the injection at a depth of 5 km (Fig. S1† & S2†) and response surface maps for time corresponding to maximum ΔP_f at 5 km depth are shown in Figure 8B,D. These results show that the maximum ΔP_f at 5 km depth tends to occur (i) before injection operations cease for the high TDS (207,000 ppm) scenarios with high permeability ($k_0 = 5 \times 10^{-13}$ m^2), (ii) after injection operations cease for the intermediate permeability scenarios ($k_0 = 1 \times 10^{-13}$m^2 and $k_0 = 5 \times 10^{-14}$ m^2), and (iii) contemporaneously with the end of the 10-year injection period for the both the low permeability scenarios ($k_0 = 1 \times 10^{-14}$ m^2) and the low TDS wastewater (107,000 ppm) scenarios. For model scenarios with high TDS wastewater and high fracture permeability, formation fluids are readily displaced as wastewater sinks (Figs. 6D,G), so advective transport of high-density wastewater is the primary mechanism driving fluid pressure accumulation. As a result, ΔP_f at 5 km depth begins rapidly increasing upon arrival of the sinking wastewater plume. When the wastewater plume passes through 5 km depth, lower density formation fluids flow back into the path of the brine plume, which, for this model scenario, occurs before injection stop (Fig. S1†). This is in stark contrast to the lowest permeability scenarios ($k_0 = 1 \times 10^{-14}$ m^2), which inhibit advective wastewater transport into the basement (Figs. 6B,E & 7B,E), so wellhead pressure diffusion is the primary process driving pressure transients into the seismogenic zone. Pressure diffusion also governs ΔP_f for model scenarios comprising wastewater with 107,000 ppm TDS because wastewater and basement fluids comprise the same TDS concentration, and thus density, at injection depth so second-order thermal effects are the only process that can cause density-driven pressure transients. For these high-permeability and low-TDS wastewater scenarios, Figure S1† and S2† show that ΔP_f increases monotonically at 5 km depth until pumping stops, which is congruent with a Theis curve. Because ΔP_f at 5 km depth is governed by advective brine transport for the high permeability scenarios and pressure diffusion for the low permeability scenarios, then pressure accumulation at 5 km depth for the intermediate permeability scenarios is the superposition of wellhead pressure and density-driven pressure transients. This superposition occurs because wastewater can enter the upper basement within the 10-year injection period (Fig. 6C,F & 7C), but formation fluid cannot be displaced as quickly as for the high permeability scenarios so wellhead pressure builds up and adds to the ΔP_f signal. When injections stop, wellhead pressure no longer contributes to the ΔP_f signal and there is a brief decline in pressure build-up; however, fluid pressure begins rising again as high-TDS wastewater accumulates between 4 and 5 km depth (Fig. S1† & S2†) where fracture permeability falls below 5×10^{-14} m^2.

The temporal dimensions of ΔP_f variations imply that basement permeability, wastewater composition and wastewater temperature each play fundamental roles in fluid pressure recovery after injection operations cease. To evaluate how far-field, diffusion-controlled pressure fronts respond during post-injection fluid pressure recovery, Figures 9A and 10A present response surface maps for maximum distance to the 10 kPa pressure front after ten years of post-injection fluid pressure recovery. This analysis indicates that far-field pressure recovery is also governed primarily by basement permeability; however, inspection of selected simulation results shows that residual fluid pressure remains locally elevated within a 1 – 2 km radius of injection wells even after 10 years of recovery, regardless of basement permeability structure (Figs. 9B-G & 10B-D). Residual fluid pressure is maintained because loading conditions imposed by high-density wastewater persist until fluid composition equilibrates with the surrounding host-rock fluids. This equilibration period is governed by fluid mixing, which is the result of both advective transport and molecular (Fickian) diffusion. In this context, advective transport slows significantly as basement permeability decreases and Fickian diffusion occurs over much longer timescales.

The persistence of residual fluid pressure in the seismogenic basement begs the question of whether or not fluid pressure continues increasing within the basement during post-injection recovery. The individual results shown in Figures 9B-G and 10B-G indicate that far-field (diffusion-controlled) pressure transients collapse in the absence of wellhead pressure. This implies that rock volume in the far field reaches maximum ΔP_f when (or soon after) injection operations cease. This result is further supported by time-series ΔP_f data recorded for each simulation at 4 km radial distance from the injection well and 4.5 km depth (Figs. S3† & S4†). The data show that ΔP_f in the far-field exhibit diffusion-

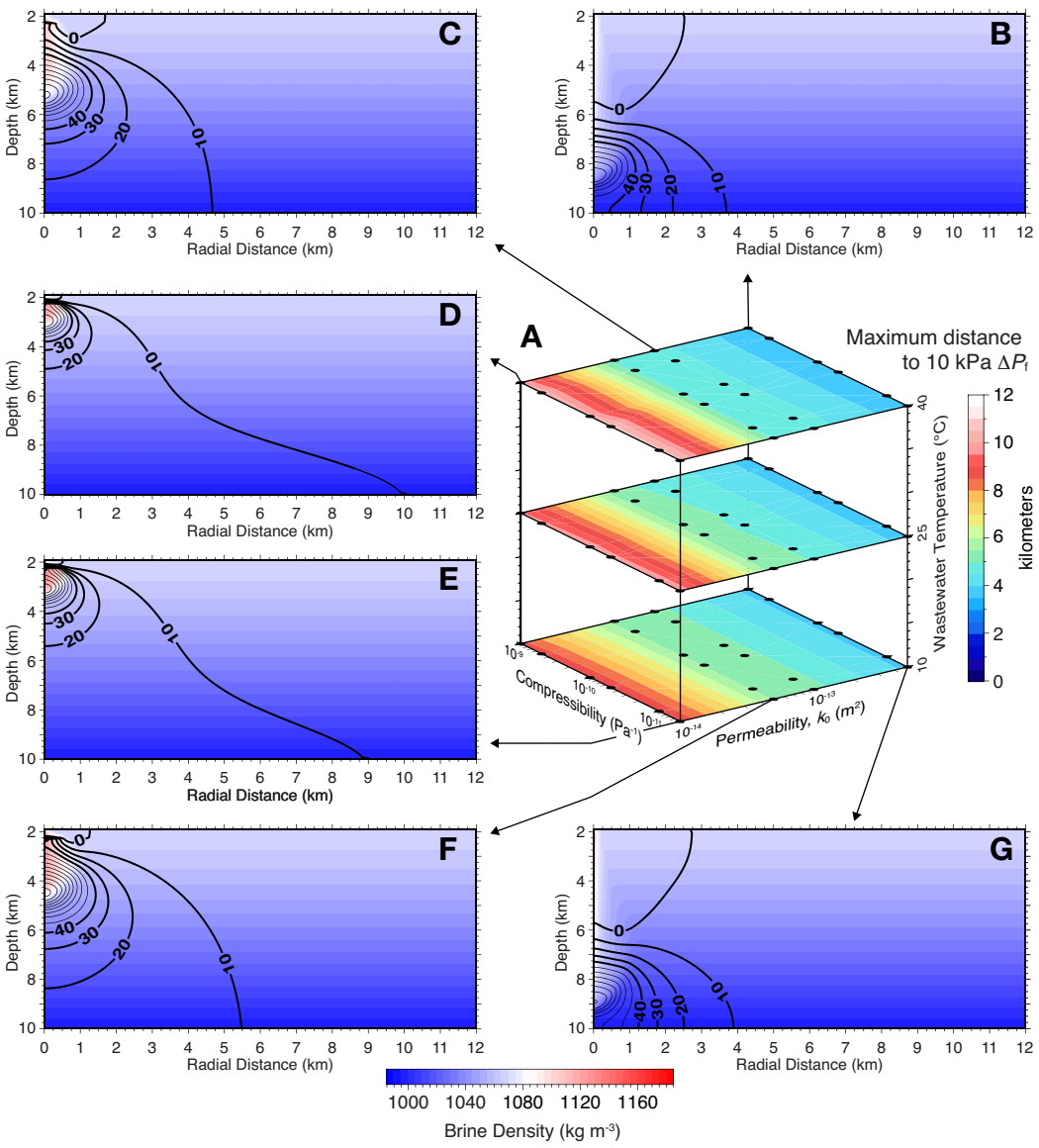

Fig. 9 Response surface analysis (A) for the maximum radial distance (km) from the injection well to the 10 kPa pressure after 10 years of post-injection fluid pressure recovery for wastewater comprising 207,000 ppm TDS and temperature of 10, 25, and 40°C. Panels B – G illustrate individual simulation results for models that bound the parameter space; black contour lines denote fluid pressure change (ΔP_f) in kPa and background shading is brine density. Contour lines greater than 40 kPa are presented with lighter stroke to facilitate visualization.

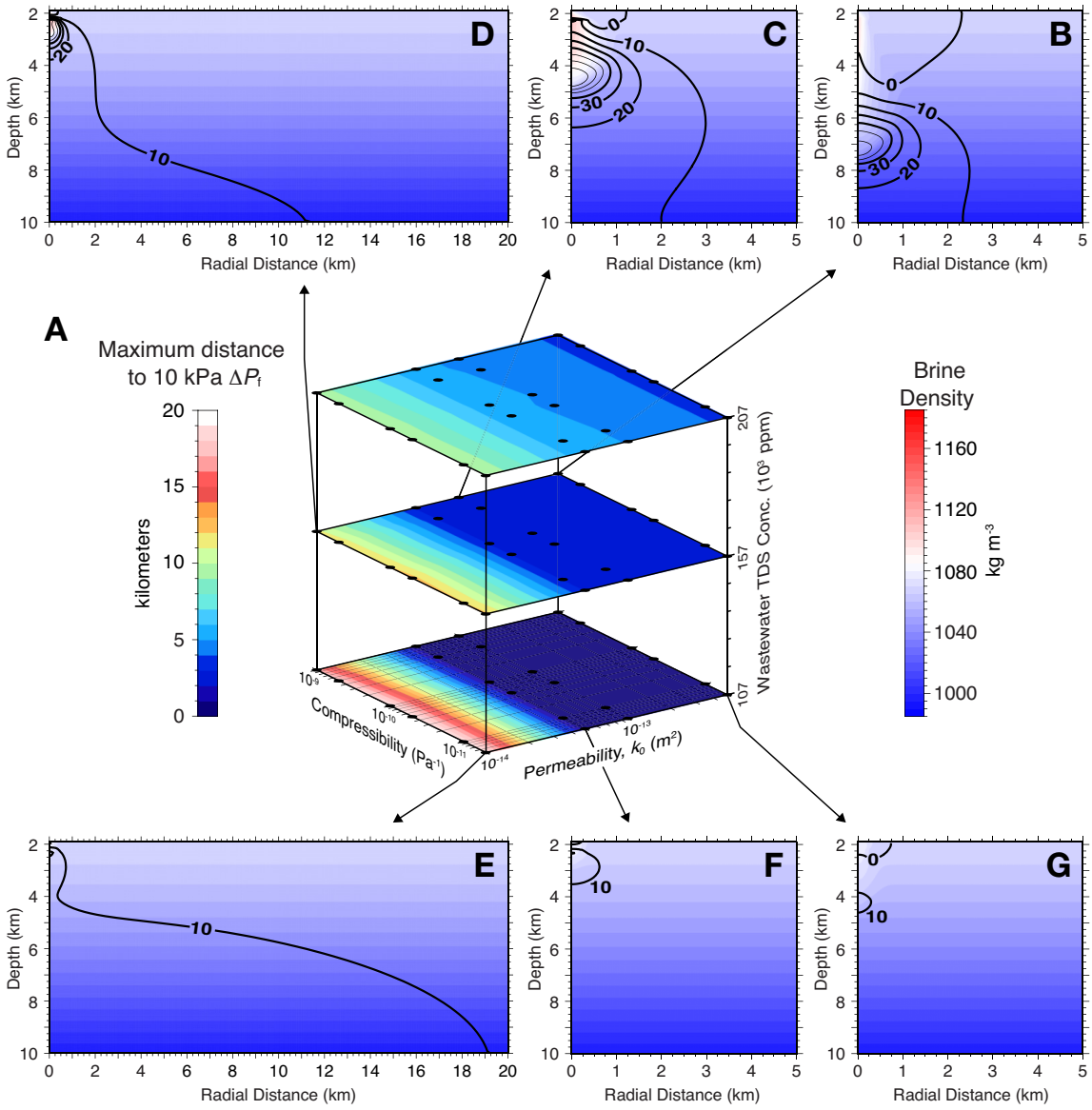

Fig. 10 Response surface analysis (A) for the maximum radial distance (km) from the injection well to the 10 kPa pressure after 10 years of post-injection fluid pressure recovery for wastewater at 25°C and brine composition of 107,000, 157,000 and 207,000 ppm TDS. Panels B – G illustrate individual simulation results for models that bound the parameter space; black contour lines denote fluid pressure change (ΔP_f) in kPa and background shading is brine density. Contour lines greater than 40 kPa are presented with lighter stroke to facilitate visualization.

controlled (Theis-like) patterns for all simulations with peak ΔP_f when injections cease. These results imply that both effective stress change and solid elastic stress transfer reach their maximum lateral extent during (or soon after) active injection operations.

Although far-field pressure transients peak during the injection period for all permeability scenarios, fluid pressure continues increasing locally below the injection well for up to 20 years after injections cease in both intermediate and high permeability scenarios (Figs. S3† & S4†). For example, ΔP_f after 10 years of injection reaches 40 kPa at 8 km depth for the high-permeability scenario illustrated in Figure 4B; however, this increases 80 kPa after a decade of recovery (Fig. 9B). This phenomenon reflects a feedback between high-TDS wastewater and the geothermal gradient because the sinking wastewater plume passes through systematically warmer and lower density host rock fluids, so the fluid density contrast driving advective pressure transients is maintained even as wastewater mixes with host rock fluids. Local regions of increasing post-injection fluid pressure also occur for the intermediate permeability scenarios, albeit at shallower depths; however, this phenomenon does not occur for the lowest permeability scenarios because wastewater cannot sink beyond the uppermost basement. In natural geologic systems, these results suggest that high-TDS wastewater may continue flowing through interconnected fault and fracture networks for years after injection operations cease. Generalizing the parametric controls on fluid pressure recovery for oilfield wastewater disposal suggests that (i) far-field pressure recovery is rapid and governed by fracture permeability, (ii) when wastewater sinks into the basement, fluid pressure continues increasing locally below injection wells even after injection operations cease, and (iii) the geothermal gradient maintains density-driven pressure transients because basement fluids become systematically warmer (and lower density) with increasing depth.

4 Discussion

There is now general consensus that wastewater disposal operations cause fluid pressure transients that induce earthquakes by (i) decreasing effective normal stresses on optimally-oriented faults and (ii) driving solid elastic stress transfer ahead of the pressure front. This study adds an important new spatiotemporal perspective to this conceptual model by integrating the effects of wastewater and basement fluid composition, the crustal scale geothermal gradient, and PTX-dependent fluid properties. Specifically, wastewater disposal operations cause long-range, diffusion-controlled pressure fronts that propagate radially in accordance with root-time scaling, while also driving solid elastic stress transfer ahead of the pressure front[10]. When wastewater comprises higher TDS concentration than basement fluids, the high-density wastewater sinks , which locally increases fluid pressure below the injection well[23] (Fig. 11A). After injection operations cease, the long-range pressure front collapses rapidly, while the density-driven pressure front continues sinking deeper into the seismogenic basement (Fig. 11B). In this context, maximum fluid pressure in the far-field occurs when (or soon after) injection operations cease, while density-driven fluid flow may continue increasing fluid pressure locally below injection wells for 10+ years.

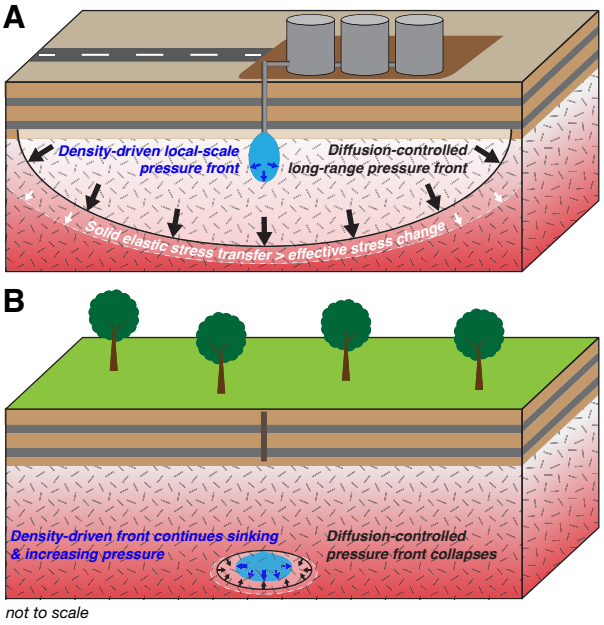

Fig. 11 Schematic illustration of mechanisms driving fluid pressure transients during oilfield wastewater disposal when (i) the disposal reservoir is hydraulically connected to crystalline basement and (ii) wastewater density is $\gtrsim 37$ kg m^{-3} greater than basement fluids due to thermal and compositional differences between the fluids. During injection operations (A), diffusion-controlled pressure transients (black arrows) propagate radially from well in accordance with root-time spatial scaling, which drives solid elastic stressing ahead of the pressure front (white arrows). As this occurs, wastewater sinks into the upper basement and density-driven pressure transients (blue shading) develop. After injection operations (B), the long-range pressure front collapses, while density-driven pressure transients continue sinking deeper into the basement. This latter process is reinforced by the natural geothermal gradient (white-to-red shading) because the density contrast between wastewater and basement fluids is maintained even as the wastewater mixes with basement fluids.

Conceptually, the timing and magnitude of density-driven pressure transients are governed by basement permeability structure and PTX conditions of wastewater and basement fluids. From a mechanistic perspective, the persistence of density-driven pressure transients is attributable to the density contrast between high-TDS wastewater and basement fluids, and this contrast increases with depth due to the natural geothermal gradient. Specifically, sinking high-TDS wastewater passes through progressively higher temperature (and thus lower density) basement fluids, which maintains the density contrast even as wastewater and basement fluids mix. Interestingly, the relationship between solid elastic stress transfer and local-scale density-driven pressure transients remains an open question, but from a qualitative perspective, it seems plausible that (i) the excess load imposed by high-TDS wastewater would increase the magnitude of solid elastic stressing locally below injection wells and (ii) density-driven pressure fronts would drive elastic stressing to systematically greater depths as the pressure front sinks. This implies that elastic stressing may persist locally over time scales that are comparable to density-driven pressure transients (Fig. 11B); however, further research is needed in this area.

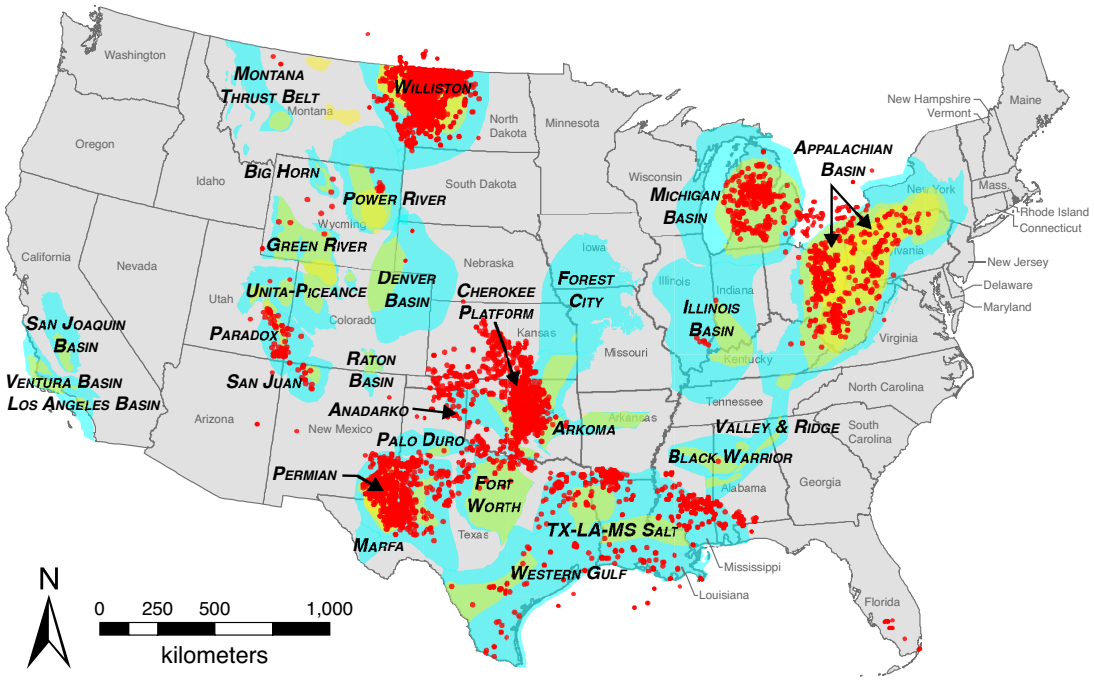

Fig. 12 Map of oil and gas basins across the coterminous United States[37] (blue shading), unconventional tight oil and shale plays[38] (yellow shading), and location of conventional hydrocarbon wells with TDS samples reported to be $\geq$200,000 ppm (red circles)[26].

In order for density-driven pressure transients to occur, wastewater must comprise higher TDS concentration than basement fluids. In this context, oilfield wastewater originates as basin brine that co-exists with oil and gas deposits in sedimentary basins. These fluids are generally considered to be remnant seawater that has been trapped within sedimentary formations since the time of deposition[39]; however, brine migration and enrichment remain active areas of research due to their relationship with oil and gas deposits and ore formation[40]. In a recent review of injection-induced seismicity, Foulger *et al.*[41] identifies several regions where wastewater disposal operations are likely to have caused earthquakes. For example, earthquake sequences in the Sichuan Basin, China have been attributed to wastewater disposal[42]. In this region, the TDS concentration of basin brine generally exceeds 150,000 ppm with several samples exceeding 300,000 ppm TDS[43]. Within the coterminous United States, where injection-induced earthquakes are now common, the USGS National Produced Waters Geochemical Database (NPWGD)[26] indicates that the TDS concentration of oilfield brine exceeds 200,000 ppm throughout many of the oil- and gas-producing basins nationwide (Fig. 12). In contrast, the NPWGD indicates that Precambrian basement fluids are characterized by lower mean TDS concentrations of ~107,000 ppm and ~39,000 ppm within the Anadarko Shelf (southern Kansas) and Permian Basin (southeastern New Mexico), respectively[26]. Although NPWGD contains only 15 records for Precambrian basement fluids (out of ~114,000 records), these data are congruent with Bucher and Stober[44] who found that basement TDS concentration is less than 100,000 ppm at 22 out of 24 international sites. These data imply that basement TDS concentration is generally below 100,000 ppm.

The numerical simulations developed for this study suggest that wastewater disposal operations may be susceptible to density-driven pressure transients if the following criteria are met: (i) basement fluids are $\lesssim$100,000 ppm TDS and oilfield brine (wastewater) is $\gtrsim$150,000 ppm TDS, although susceptibility increases dramatically for TDS concentration $\gtrsim$200,000 ppm TDS; (ii) wastewater disposal wells are in hydraulic connection with the underlying basement; and (iii) basement fracture permeability is $\gtrsim 5 \times 10^{-14}$ m^2. Although basement fracture permeability is generally unknown, oilfield brine is characterized by TDS concentration in excess of 150,000 ppm throughout numerous oil and gas basins worldwide, e.g., Sichuan Basin, China[43], Baltic Basin, Poland[45], Northwest Carboniferous Basin, UK[46], Paris Basin, France[47], to name a few. In the central United States, numerous unconventional oil and gas plays occur in sedimentary basins with brine composition reported to be in excess of 200,000 ppm TDS, e.g., Permian and Anadarko Basins[26] (Fig. 12). Because basement fluids are generally below 100,000 ppm TDS[26,44], oilfield wastewater disposal in basins with $\gtrsim$200,000 ppm TDS brine (Fig. 12) may be susceptible to the long-term effects of density-driven pressure transients if disposal wells are in hydraulic communication with the underlying basement. This susceptibility is particularly relevant for unconventional plays (tight oil and shale gas) because they are characterized by low permeability, so produced brine cannot be reinjected back into the producing formation (i.e., waterflooding). As a result, brine produced from unconventional hydrocarbon recovery is reinjected into non-producing geologic formations, which may result in fluid pressure transients that trigger earthquakes.

The most prominent case study for injection-induced seismicity is the State of Oklahoma, USA, where the annual M3+ earthquake rate increased from approximately one per year before 2009 to more then two M3+ earthquakes per day in 2015[6]. It is now well-known that oilfield wastewater disposal from unconventional plays contributed to this dramatic rise in earthquake frequency[3,4,6]. In this region, oilfield brine from the Mississippi Lime and Hunton formations is characterized by ∼175,000 to 235,000 ppm TDS[23,26]. These fluids are then reinjected into the basal Arbuckle formation, which is in hydraulic communication with the seismogenic basement[5]. And while earthquake frequency peaked in 2015[6], recent research shows that density-driven pressure transients from high-TDS wastewater continue driving earthquakes systematically deeper[23]. Based on these criteria, the Permian Basin (Fig. 12) may also be susceptible to the effects of density-driven pressure transients because (i) unconventional oil and gas production, wastewater disposal, and earthquake occurrence have been increasing steadily since 2015[48]; (ii) the water cut (ratio of produced brine to total fluid withdrawals) is ∼70%[49]; and (iii) wastewater disposal occurs in the Ellenburger Group[50], which is a deep carbonate platform sequence that is juxtaposed with the underlying basement. In contrast, the Williston and Appalachian Basins (Fig. 12) may be less susceptible to density-driven pressure transients because there are fewer wastewater disposal wells in operation and the water cut is low in comparison to the Permian Basin and Anadarko Shelf[49,51].

5 Conclusions

There is now ample evidence to suggest that oilfield wastewater disposal induces fluid pressure transients that cause earthquakes by (i) decreasing effective normal stress on optimally-oriented faults (e.g., [5,35]) and (ii) driving solid elastic stress transfer ahead of the pressure front (e.g., [7,10]). This implies that fluid pressure transients are the first-order process responsible for injection-induced earthquakes. Numerous modeling studies show that pressure diffusion drives long-range fluid pressure transients during oilfield wastewater disposal[5,7,11,13,15,17,19,22]; however, Pollyea *et al.* [23] recently found that density-driven fluid flow also drives pressure transients into the seismogenic zone when there is a strong density contrast between wastewater and basement fluids. The present study implements ensemble simulation methods to isolate the hydraulic, thermal, geochemical, and geologic controls on both diffusion-controlled and density-driven fluid pressure transients. For wastewater disposal wells that are in hydraulic communication with underlying basement, results from this study can be generalized as:

1. Long-range, diffusion-controlled pressure transients are governed by basement fracture permeability, but they are generally insensitive to wastewater chemistry, injection temperature and basement fracture compressibility;

2. Density-driven pressure transients are dependent on the density differential between wastewater and basement fluids and require sufficient basement fracture permeability to allow density-driven fluid flow. Results from this study suggest that density-driven pressure transients may develop when the following criteria are met: (i) basement fracture permeability is $\gtrsim 5 \times 10^{-14}$ m^2 at seismogenic depth, (ii) basement fluid composition is $\lesssim$100,000 ppm TDS, and (iii) wastewater comprises $\gtrsim$150,000 ppm TDS ; however, the depth and magnitude of density-driven pressure transients increases dramatically when wastewater TDS concentration exceeds 200,000 ppm;

3. When wastewater injections cease, the absence of wellhead pressure causes far-field (diffusion-controlled) pressure fronts to collapse rapidly; however, density-driven pressure transients continue to locally increase fluid pressure at systematically greater depths for 10+ years;

4. The long-term persistence of density-driven pressure transients is reinforced by the crustal-scale geothermal gradient because high-TDS wastewater sinks through systematically warmer (and lower density) basement fluids, thus maintaining the fluid density contrast;

5. Wastewater temperature is a second-order control on the depth and magnitude of density-driven pressure transients because (i) cooler wastewater comprises higher density, which increases the dynamic load and (ii) basement fluid density decreases with depth as temperature increases.

These conclusions present a new perspective on the hydraulics of induced seismicity by accounting for wastewater chemistry, PTX-dependent fluid properties and depth-varying geologic properties. This new perspective enhances the generally accepted conceptual model of injection-induced seismicity by incorporating the effects of density-driven pressure transients, which continue migrating through seismogenic zone long after injection operations cease[23]. This new conceptual model (Fig. 11) is applicable to oil and gas basins where oilfield wastewater is characterized by $\gtrsim$150,000 ppm TDS, which are widespread globally.

In closing this study, it is important to state clearly that the model scenario developed herein is based on numerous geologic and operational characteristics of the Anadarko Shelf; however, the model itself is hypothetical and does not reproduce a real world site. In addition, the geology reproduced in this study is highly idealized because site-scale fracture networks in the crystalline basement are poorly characterized in comparison with resource-bearing sedimentary formations. As a result, this study yields insights about the physics governing injection-induced pressure transients, and thus effective stress change. In natural geologic systems, the spatial patterns of density-driven pressure transients will be strongly dependent on heterogeneous and anisotropic hydraulic properties of basement fracture networks and they are likely to vary in comparison to the idealized schematic presented in Figure 11. As a result, the application of this study for site-scale earthquake hazard analysis requires substantial investments for characterizing the hydraulic attributes of the seismogenic basement. Because injection-induced pressure transients are a fundamental component of numerous geoenergy technologies, e.g., enhanced geothermal systems[52] and geologic carbon sequestration[53], the authors hope that insights gained

from this study further motivate frontier research into the hydraulic characteristics of faults and fractures in the seismogenic basement.

Conflicts of interest

There are no conflicts to declare.

Acknowledgements

The authors thank Dr. Martin C. Chapman for insightful discussions about injection-induced earthquakes. The authors are grateful to two anonymous reviewers who provided thoughtful comments that dramatically improved the quality of this manuscript. Computational resources were provided by Advanced Research Computing at Virginia Tech. This study is based upon work supported by the U.S. Geological Survey under Grant No. G19AP00011. The views and conclusions contained in this document are those of the authors and should not be interpreted as representing the opinions or policies of the U.S. Geological Survey. Mention of trade names or commercial products does not constitute their endorsement by the U.S. Geological Survey.

Notes and references

1 W. L. Ellsworth, *Science*, 2013, **341**, 1225942.
2 S. E. Hough, *Bulletin of the Seismological Society of America*, 2014, **104**, 2619–2626.
3 M. Weingarten, S. Ge, J. W. Godt, B. A. Bekins and J. L. Rubinstein, *Science*, 2015, **348**, 1336–1340.
4 K. M. Keranen, H. M. Savage, G. A. Abers and E. S. Cochran, *Geology*, 2013, **41**, 699–702.
5 K. M. Keranen, M. Weingarten, G. A. Abers, B. A. Bekins and S. Ge, *Science*, 2014, **345**, 448–451.
6 R. M. Pollyea, N. Mohammadi, J. E. Taylor and M. C. Chapman, *Geology*, 2018, **46**, 215–218.
7 T. Goebel, M. Weingarten, X. Chen, J. Haffener and E. Brodsky, *Earth and Planetary Science Letters*, 2017, **472**, 50–61.
8 NRC, *Induced Seismicity Potential in Energy Technologies*, National Academies Press, 2013.
9 P. Bhattacharya and R. C. Viesca, *Science*, 2019, **364**, 464–468.
10 T. H. Goebel and E. E. Brodsky, *Science*, 2018, **361**, 899–904.
11 G. Zhai, M. Shirzaei, M. Manga and X. Chen, *Proceedings of the National Academy of Sciences*, 2019, **116**, 16228–16233.
12 S. L. Peterie, R. D. Miller, J. W. Intfen and J. B. Gonzales, *Geophysical Research Letters*, 2018, **45**, 1395–1401.
13 R. M. Pollyea, *Hydrogeology Journal*, 2020, **28**, 795–803.
14 C. Langenbruch, M. Weingarten and M. D. Zoback, *Nature Communications*, 2018, **9**, 1–10.
15 Y. Zhang, M. Person, J. Rupp, K. Ellett, M. A. Celia, C. W. Gable, B. Bowen, J. Evans, K. Bandilla, P. Mozley *et al.*, *Groundwater*, 2013, **51**, 525–538.
16 M. R. Brown and S. Ge, *Geophysical Research Letters*, 2018, **45**, 5445–5453.
17 E. H. Hearn, C. Koltermann and J. L. Rubinstein, *Geochemistry, Geophysics, Geosystems*, 2018, **19**, 1178–1198.
18 J. H. Norbeck and R. N. Horne, *Tectonophysics*, 2018, **733**, 108–118.
19 J. Norbeck and J. L. Rubinstein, *Geophysical Research Letters*, 2018, **45**, 2963–2975.
20 P. O. Ogwari, H. R. DeShon and M. J. Hornbach, *Journal of Geophysical Research: Solid Earth*, 2018, **123**, 553–563.
21 M. Schoenball, F. R. Walsh, M. Weingarten and W. L. Ellsworth, *The Leading Edge*, 2018, **37**, 100–106.
22 C. Langenbruch and M. D. Zoback, *Science Advances*, 2016, **2**, year.
23 R. M. Pollyea, M. C. Chapman, R. S. Jayne and H. Wu, *Nature Communications*, 2019, **10**, 1–10.
24 C. Manning and S. Ingebritsen, *Reviews of Geophysics*, 1999, **37**, 127–150.
25 Y. I. Klyukin, R. Lowell and R. Bodnar, *Fluid Phase Equilibria*, 2017, **433**, 193–205.
26 M. Blondes, K. Gans, M. Engle, Y. Kharaka, M. Reidy, V. Saraswathula, J. Thordsen, E. Rowan and E. Morrissey, *U.S. Geological Survey National Produced Waters Geochemical Database (ver. 2.3, January 2018)*, 2018, U.S. Geological Survey data release.
27 K. S. Johnson, *Oklahoma Geological Survey Circular*, 1991, **92**, 3–14.
28 C. Cranganu, Y. Lee and D. Deming, *Journal of Geophysical Research: Solid Earth*, 1998, **103**, 27107–27121.
29 Y. Jung, G. S. H. Pau, S. Finsterle and R. M. Pollyea, *Computers & Geosciences*, 2017, **108**, 2–7.
30 P. A. Domenico, F. W. Schwartz *et al.*, *Physical and chemical hydrogeology*, Wiley New York, 1998, vol. 506.
31 I. T. Kukkonen and C. Clauser, *Geophysical Journal International*, 1994, **116**, 409–420.
32 J. Townend and M. D. Zoback, *Geology*, 2000, **28**, 399–402.
33 R. M. Pollyea, *International Journal of Greenhouse Gas Control*, 2016, **46**, 7–17.
34 W. L. Yeck, L. V. Block, C. K. Wood and V. M. King, *Geophysical Journal International*, 2015, **200**, 322–336.
35 M. R. Brown, S. Ge, A. F. Sheehan and J. S. Nakai, *Journal of Geophysical Research: Solid Earth*, 2017, **122**, 6569–6582.
36 P. A. Reasenberg and R. W. Simpson, *Science*, 1992, **255**, 1687–1690.
37 USEIA, *Sedimentary basin boundaries in Lower 48 States (shapefile)*, `https://www.eia.gov/maps/map_data/SedimentaryBasins_US_EIA.zip`, 2016, Accessed: 2020-03-12.
38 USEIA, *Low permeability oil and gas play boundaries in Lower 48 States (shapefile)*, `https://www.eia.gov/maps/map_data/TightOil_ShaleGas_Plays_Lower48_EIA.zip`, 2019, Accessed: 2020-03-12.
39 M. Musgrove and J. L. Banner, *Science*, 1993, **259**, 1877–1882.
40 G. Ferguson, J. C. McIntosh, S. E. Grasby, M. J. Hendry, S. Jasechko, M. B. Lindsay and E. Luijendijk, *Geophysical Research Letters*, 2018, **45**, 4851–4858.
41 G. R. Foulger, M. P. Wilson, J. G. Gluyas, B. R. Julian and R. J.

Davies, *Earth-Science Reviews*, 2018, **178**, 438–514.
42 X. Lei, G. Yu, S. Ma, X. Wen and Q. Wang, *Journal of Geophysical Research: Solid Earth*, 2008, **113**, year.
43 Z. Xun, L. Cijun, J. Xiumin, D. Qiang and T. Lihong, *Groundwater*, 1997, **35**, 53–58.
44 K. Bucher and I. Stober, *Geofluids*, 2010, **10**, 241–253.
45 V. Raidla, K. Kirsimäe, R. Vaikmäe, A. Jõeleht, E. Karro, A. Marandi and L. Savitskaja, *Chemical Geology*, 2009, **258**, 219–231.
46 A. A. Holland, *Bulletin of the Seismological Society of America*, 2013, **103**, 1784–1792.
47 J.-M. Matray and J.-C. Fontes, *Geology*, 1990, **18**, 501–504.
48 R. J. Skoumal, A. J. Barbour, M. R. Brudzinski, T. Langenkamp and J. O. Kaven, *Journal of Geophysical Research: Solid Earth*, 2020, **125**, e2019JB018558.
49 B. R. Scanlon, M. B. Weingarten, K. E. Murray and R. C. Reedy, *Seismological Research Letters*, 2019, **90**, 171–182.
50 C. R. Lemons, G. McDaid, K. M. Smye, J. P. Acevedo, P. H. Hennings, D. A. Banerji and B. R. Scanlon, *Environmental Geosciences*, 2019, **26**, 107–124.
51 B. R. Scanlon, S. Ikonnikova, Q. Yang and R. C. Reedy, *Environmental Science & Technology*, 2020, **54**, 3510–3519.
52 M. White, T. Johnson, T. Kneafsey, D. Blankenship, P. Fu, H. Wu, A. Ghassemi, J. Lu, H. Huang, G. Neupane *et al.*, Proceedings 44th Workshop on Geothermal Reservoir Engineering, Stanford University, 2019.
53 R. S. Jayne, H. Wu and R. M. Pollyea, *International Journal of Greenhouse Gas Control*, 2019, **83**, 128–139.

Broader Context: EE-ART-06-2020-001864

A new perspective on the hydraulics of oilfield wastewater disposal: How PTX conditions affect fluid pressure transients that cause earthquakes

Ryan M. Pollyea, Graydon L. Konzen, Cameron R. Chambers, Jordan A. Pritchard, Hao Wu, and Richard S. Jayne

(200 word max)

Oil and gas production is often accompanied by highly brackish waste fluids that are disposed of by reinjection into deep geologic formations. This process causes earthquakes when injection-induced fluid pressure transients destabilize faults through a combination of effective stress change and elastic stress transfer. This conceptual model has been developed on the basis of modeling studies that assume pressure diffusion is the only mechanistic process driving fluid pressure transients into the seismogenic basement. However, recent research shows that oilfield wastewater comprising substantially higher total dissolved solids (TDS) concentration than basement fluids results in density-driven fluid pressure transients that sink and drive earthquakes systematically deeper. This means that pressure, temperature, and composition (PTX) conditions of both wastewater and basement fluids plays a fundamental role in the hydraulic processes that cause earthquakes. This study develops a new mechanistic framework for the hydraulics of oilfield wastewater disposal by integrating PTX-dependent fluid properties into the generally accepted conceptual model of injection-induced seismicity. Using nonisothermal, variable-density numerical simulation, results from this study show that density-driven pressure transients may emerge when wastewater TDS concentration is ~50,000 ppm greater than basement fluids, which is a common occurrence throughout oil and gas basins worldwide.